Comparison of Coastal and Regional Ocean Community Model (CROCO) and NCAR-LES in Non-hydrostatic Simulations

Xiaoyu Fan

Department of Earth, Environmental, and Planetary Sciences, Brown University

Abstract.

Coastal and Regional Ocean COmmunity model (CROCO) and NCAR Large-eddy simulations (NCAR-LES) are compared with a focus on their accuracy and efficiency. In accuracy comparison, we compared the turbulence statistics, including the effect of the explicit SGS parameterization, the effect of the second viscosity parameter, the sensitivity to the speed-of-sound parameter and the sensitivity to the time step. In addition, we compared CROCO simulations with NCAR-LES cases of (Li and Fox-Kemper, 2017) with various combinations of surface wind and surface cooling. To test the performance of NCAR-LES, we compared it with two other versions of LES. In efficiency comparison, the pure computing time is recorded to measure the model efficiency. Strong and weak scaling simulations are set for different problem sizes and workload per processor respectively. 2D decomposition of CROCO and NCAR-LES is discussed; settings of the Cheyenne supercomputer are tested.

1 Introduction

Coastal and Regional Ocean Community model (CROCO) is built on ROMS_AGRIF and the non-hydrostatic kernel of SNH to resolve very fine-scale coastal area (Debreu et al., 2016). From basic fluid mechanics equations, Equation1 shows the vertical momentum equation in the w component that can explain the hydrostatic balance. This means that the pressure is the only term could balance the gravitational term in hydrostatic balance.

$$\frac{\partial p}{\partial z} = -\rho g \tag{1}$$

In Boussinesq fluid, the buoyancy mainly drives the motion, so the hydrostatic balance equation can be written as Equation 2, which means that the advective term is the combination of pressure gradient and buoyancy.

$$\frac{Dw}{Dt} = -\frac{\partial \phi}{\partial z} + b \tag{2}$$

When the advective term is divided by the pressure gradient term, the condition of hydrostasy shows in Equation3. Alpha is the aspect ratio meaning the vertical scale versus the horizontal scale, which is much less than one. This situation is called hydrostatic balance meaning the vertical component is much less than horizontal component and can be neglected.

$$\alpha^2 = (\frac{H}{L})^2 \ll 1 \tag{3}$$

The non-hydrostatic model is necessary for the study of ocean small-scale phenomena in non-hydrostatic balance, which adopts full incompressible Navier-Stokes equations (Marshall et al., 1997). In non-hydrostatic balance, the aspect ratio approaches 1 as in Equation 4, both horizontal and vertical dimensions are simulated importantly, meaning the motion of turbulence is on the same scale for each direction.

$$(\frac{H}{L})^2 \sim 1 \tag{4}$$

The resolution of CROCO greatly various. CROCO enables extremely high resolution simulations in this study up to about 1m; while the other applications to solve practical problems at small- or meso-scale ocean problems, such as coupling with biogeochemical model, are applying the resolution of more than 1km.

In this paper, CROCO simulation results are validated with Large-Eddy-Simulation (LES) model. LES is an idealized fluid dynamics model but it can't be used with realistic complicated topography. NCAR-LES, PALM and Oceananigan are branches of LES model: NCAR-LES is developed by NCAR (Moeng, 1984). PALM was developed as a turbulence-resolving LES model for atmospheric and oceanic boundary layer flows, specifically designed to run on massively parallel computer architectures (https://palm.muk.uni-hannover.de/trac). In this paper, these three types of LES model are compared in accuracy comparison section to assess the performance of NCAR-LES, because NCAR-LES is mainly applied for the comparison with CROCO.

In this paper, the comparisons are divided into two major aspects: accuracy comparison and efficiency comparison. In accuracy comparison, the turbulence statistics are used for comparison, including the effect of the explicit SGS parameterization, the effect of the second viscosity parameter, the sensitivity to the speed-of-sound parameter and the sensitivity to the time step. In addition, the CROCO simulations are compared with NCAR-LES cases of (Li and Fox-Kemper, 2017) with various combinations of surface wind and surface cooling. In efficiency comparison, the computing time for each time step is recorded to measure the model efficiency. Strong and weak scaling simulations are respectively set for different problem sizes and workload per processor. 2D decomposition of CROCO and NCAR-LES and the settings of the Cheyenne supercomputer are discussed.

2 Turbulence statistics comparison

In this section, we compare the turbulence statistics simulated by the NCAR boundary-layer LES model (Moeng, 1984; Sullivan et al., 1994; Sullivan and Patton, 2011) and the Coastal and Regional Ocean Community (CROCO) non-Boussinesq (NBQ) model (Auclair et al., 2018; Marchesiello et al., 2021). In addition, we test the sensitivity to the values of certain constants specific to the CROCO NBQ model.

All simulations here use the following configuration. The grid has 256 uniformly-spaced points in each direction. The domain size is $320\,\mathrm{m} \times 320\,\mathrm{m}$ horizontally and $163.84\,\mathrm{m}$ vertically. The horizontal resolution $\Delta x = \Delta y$ is $1.25\,\mathrm{m}$, and the vertical resolution Δz is $0.64\,\mathrm{m}$. The vertical Coriolis parameter f is $1.028 \times 10^{-4}\,\mathrm{s}^{-1}$, and the horizontal Coriolis parameter is $0\,\mathrm{s}^{-1}$. The density ρ is given by the linear equation of state without salinity: namely, $\rho = \rho_0 + \rho_0 \beta_T (\theta_0 - \theta)$ with the reference density $\rho_0 = 1000\,\mathrm{kg\,m}^{-3}$, reference temperature $\theta_0 = 13.554\,^{\circ}\mathrm{C}$, the thermal expansion coefficient $\beta_T = 2 \times 10^{-4}\,^{\circ}\mathrm{C}^{-1}$, and

temperature θ. Initially, there is a mixed layer having $\theta = 14\,^{\circ}\mathrm{C}^{-1}$ above $z \geq -42\,\mathrm{m}$, and below that depth the temperature linearly decreases to $12.8\,^{\circ}\mathrm{C}^{-1}$ at $z = 163.84\,\mathrm{m}$. The bottom boundary uses a rigid free-slip surface and no-flux conditions. At the upper-boundary, uniform wind stress in the x-direction and uniform surface heat flux Q_* are applied where the upper-boundary temperature flux is given by $Q_*/(\rho_0 c_p)$ with specific heat capacity $c_p = 3985\,\mathrm{J\,kg^{-1}\,^{\circ}C^{-1}}$. The gravitational acceleration g is $9.81\,\mathrm{m\,s^{-2}}$. During the initial spin-up period, the wind stress and the surface heat flux increase to their full values over 51 minutes (5% of the inertial period). After this period, they stay constant. Four combinations of the water-side friction velocity U_* and the surface heat flux Q_* are considered: namely, $(U_*, Q_*) = (0.006\,\mathrm{m\,s^{-1}},\, 5\,\mathrm{W\,m^{-2}})$, $(0.006\,\mathrm{m\,s^{-1}},\, 50\,\mathrm{W\,m^{-2}})$, $(0.012\,\mathrm{m\,s^{-1}},\, 5\,\mathrm{W\,m^{-2}})$, and $(0.012\,\mathrm{m\,s^{-1}},\, 50\,\mathrm{W\,m^{-2}})$.

The NCAR LES model uses a two-part SGS eddy-viscosity model of Sullivan et al. (1994) designed to improve the LES accuracy near the surface at $z = 0\,\mathrm{m}$. Their SGS model constants C_k and C_ϵ in their equations 4 and 11 are 0.1 and 0.93, respectively. We configure their SGS model such that it reduces to a simpler form (their equation 1) below $z = -21\,\mathrm{m}$. With rough approximations, this simpler model can be related to the Smagorinsky model with a relatively large value of the corresponding Smagorinsky constant $C_s = 0.18$ (their equation 14). The NCAR LES uses the pseudo-spectral method (Fox and Orszag, 1973) for the horizontal derivatives and the second-order centered finite-differences for the vertical derivatives (Moeng, 1984). The resolved vertical temperature flux is determined using a second-order near monotone scheme (Beets and Koren, 1996). The higher one-third wavenumbers are truncated so that the aliasing error does not exists (Orszag, 1971). The time stepping utilizes a third-order Runge-Kutta scheme (Sullivan et al., 1996). More information is given in Moeng (1984); Sullivan et al. (1994); Sullivan and Patton (2011).

The CROCO NBQ model offers several options for the SGS parameterizations. In this paper, we consider two options: namely, the use of only numerical diffusion and the SGS model based on Lilly (1962). The former avoids adding any explicit SGS terms and implicitly relies only on numerical diffusion. Here, the WENO5-Z improved version of the 5th-order weighted essentially nonoscillatory scheme (Borges et al., 2008) is used for all advection terms (see Auclair et al., 2018; Marchesiello et al., 2021, for more information). Unless explicitly mentioned otherwise, the CROCO runs shown here use the former option for the SGS parametrization because we are interested in understanding the performance of (unavoidable) numerical diffusion before adding explicit SGS terms (and associated parameters) and making the model behavior more complex. We test the explicit SGS effect only briefly in section 2.2.

2.1 NCAR LES model vs CROCO NBQ model

Here, we compare the NCAR LES model with the CROCO NBQ model. As we will see shortly, the results show that these two models produce very similar boundary-layer flows.

The CROCO model uses a time-splitting method and uses two different time steps for the so-called fast and slow modes. In this subsection, all of the CROCO runs use a slow-mode time-step of $0.5\,\mathrm{s}$ and a fast-mode time-step of $0.019\,\mathrm{s}$. We tested many different time steps, and these values seem largest stable values for the configuration used. To match this slow-mode time step, the NCAR model runs in this section use a time-step of $0.5\,\mathrm{s}$ as well. However, note that the NCAR model can be run

with a much larger time step; namely, the Courant-Friedrichs-Lewy (CFL) time-step of the NCAR runs are about $7\,\mathrm{s}$ for the run with $U_* = 0.006\,\mathrm{m\,s^{-1}}$ and about $3\,\mathrm{s}$ for the runs with $U_* = 0.012\,\mathrm{m\,s^{-1}}$.

The CROCO NBQ model has two constants related to the fast mode: namely, the speed of sound c_s and the second viscosity (also called bulk viscosity, volume viscosity, or dilatational viscosity) λ. Because we are not interested in sound waves, we may use an unphysically-small value of c_s and an unphysically-large value of λ to relax the sound-related CFL constraint. In this subsection, we use $c_s = 3\,\mathrm{m\,s^{-1}}$ and $\lambda = 1\,\mathrm{kg\,s^{-1}\,m^{-1}}$. As shown in sections 2.4 and 2.3, the unphysical values of these constants affect turbulence statistics negligibly.

Figures 1 and 2 show the vertical profiles of various flow properties.[1] Hereafter, we use the following symbols: the horizontal average $\overline{\phi}$ and the turbulent fluctuation $\phi' \equiv \phi - \overline{\phi}$ for any quantity ϕ, the buoyancy $b \equiv -g\rho/\rho_0$, the buoyancy frequency $N^2 \equiv \partial\overline{b}/\partial z$, and the horizontally-averaged depth z_p of the mixed-layer base defined as the z-coordinate of the N^2 maximum.

To understand these figures, let us first explain the nondimensionalization used. Figures 1a, 2a, 2b, 2c, and 2f show quantities related to the turbulent kinetic energy (TKE) and the TKE shear production such as the mean shear and a Reynolds stress component. These quantities are largely governed by the energy input to the water rather than the wind stress or surface heat flux. Therefore, we introduce a characteristic scale E_* of the surface energy flux:

$$E_* \equiv U_*^2 \overline{u}_0 + B_* |z_p| \tag{5}$$

where $\overline{u}_0(t) \equiv \overline{u(x, y, z = 0, t)}$ is the surface current in the wind-stress direction, and $B_* \equiv g\beta_T Q_*/(\rho_0 c_p)$ is the surface buoyancy flux. The first term on the r.h.s. is the flux of the work done by the wind stress, and the second term is a rough approximation of the flux of available potential energy.[2] For ease of notation, we use an energy-flux-based velocity scale

$$U_E \equiv E_*^{\frac{1}{3}}. \tag{6}$$

While $\overline{v}$ and $\overline{u'w'}$ are also related to the TKE shear production, they are largely constrained by other factors. Therefore, we use other scalings to nondimensionalize them. Namely, figure 1b uses the vertically-averaged Ekman transport velocity $U_*^2/(f|z_p|)$ because $\overline{v}$ is roughly constrained by the Ekman balance. Figure 2e uses the wind stress U_*^2 because $\overline{u'w'}$ is constrained by the wind stress.

In figure 1d, we use a stratification scale Γ_N pertinent to pycnocline entrainment where

$$\Gamma_N \equiv \frac{2E_b^{\frac{2}{3}}}{\Delta_e(z_w - z_p)}, \tag{7}$$

and Δ_e is a length scale[3], and

$$z_w \equiv -\frac{U_E}{4.5f} \tag{8}$$

[1] Each profile is an average of 21 samples taken every one-fortieth (about 25 minutes) of the inertial period during $t = 4.7$ to 13.6 hours. At each given time, the normalized profiles are computed using the characteristic scales at that time. Then, the final profiles are made by averaging these normalized profiles. The time window is kept short, about 9 hours, because the simulated flow is not in a statistically steady state due to mixed-layer deepening. In all simulations, the boundary-layer thickness reaches the initial mixed-layer thickness within 4 hours from $t = 0\,\mathrm{s}$ when the flow has no motion.

[2] Here, for notational simplicity, we use a positive value when energy is coming into the water.

[3] The length scale Δ_e is independent of the flow. Therefore, an arbitrary value may be used. Here we arbitrarily use $\Delta_e = 1\,\mathrm{m}$.

is a rough depth scale of the wind-driven boundary layer[4], and

$$E_b \equiv U_*^2 \overline{u}_0 e^{-\frac{z_p}{z_w}} + B_* |z_p| \tag{9}$$

is a rough scale of the energy flux at z_p causing pycnocline entrainment.[5] Unlike the available potential energy input, the wind energy input is largely dissipated near the surface and is not directly used for pycnocline entrainment. Therefore, (9) assumes an exponential decay of the wind energy available to pycnocline entrainment. Note that, for a pycnocline buoyancy frequency N_p^2, $(z_w - z_p)\Delta_e N_p^2/2$ is the energy necessary to mix Δ_e thickness of the pycnocline water with the adjacent mixed-layer water located between z_w and z_p where mostly the convective turbulence has to entrain the pycnocline water and lift it up to the Ekman-layer bottom z_w (where a larger amount of wind energy is available to the mixing above). Therefore, the normalized buoyancy frequency in figure 1d indicates how strong the pycnocline stratification is relative to the energy input available for the pycnocline entrainment.

In figure 1e, we use a two-part buoyancy flux scale

$$\Gamma_{b'w'} \equiv \max\Big(1 - \frac{z}{z_p},\, 0\Big) B_* + \min\Big(\frac{z}{z_p},\, 1\Big)\, E_b^{\frac{2}{3}} \sqrt{N_p^2} \times 4 \times 10^{-3} \tag{10}$$

where the first term is the scale relevant near the surface and the second term is the scale relevant near the boundary-layer bottom. The nondimensional constant 4×10^{-3} in the second term is used only to make the normalized value at z_p close to -1.

Figure 1f uses the energy-flux-based scale for $w'w'w'$ but modified with a nondimensional function ϕ_s as

$$\Gamma_{w'w'w'} \equiv \phi_s U_E^3 \tag{11}$$

because $w'w'w'$ is very sensitive to the turbulence structure. When $(U_*, Q_*) = (0.006\,\mathrm{m\,s^{-1}}, 50\,\mathrm{W\,m^{-2}})$, the turbulence develops distinct convective rolls spanning the whole boundary-layer depth while in other cases convective rolls are much weaker and the turbulence structures in the upper part of the boundary layer are more similar to the pure wind-driven turbulence–which mainly consists of smaller-scale and more-disturbed tilted-vortexes–and the turbulence structures in the lower part of the boundary layer are similar to pure convective plumes. Convective rolls utilize both wind energy and available potential energy constructively and channel these energies into bands of strong w'. In contrast, the turbulence in the other cases uses wind energy to mix the water in the upper part of the boundary layer and thereby partially distracts the available potential energy coming in from the surface. As a result, $\overline{w'w'w'}$ due to convective rolls is much stronger. Therefore, to make the order of the normalized values similar, we use $\phi_s = 5$ when $(U_*, Q_*) = (0.006\,\mathrm{m\,s^{-1}}, 50\,\mathrm{W\,m^{-2}})$ and $\phi_s = 1$ otherwise.

Figure 2d shows $\overline{b'b'}$ near z_p. It is dominated by internal waves and isopycnal deformation due to the boundary-layer turbulence reaching z_p. The nondimensionalization is done relative to the stratification and the energy input to these processes:

[4]The factor 4.5 is an empirical nondimensional coefficient. Equation (8) is related to the standard thickness of the Ekman layer derived assuming a constant vertical eddy viscosity. Here, however, we relate the wind-driven boundary-layer thickness to the surface energy flux because the eddy viscosity does not have to be vertically uniform but is still roughly related to the surface energy flux.

[5]When the wind energy mixes the surface water very well and thereby siginificantly distract the available potential energy due to the surface cooling, it may be more appropriate to use $B_*|(z_w - z_p)|$ instead in the second term.

namely,

$$\Gamma_{b'b'} \equiv E_b^{\frac{2}{3}} N^2. \tag{12}$$

Figures 1a, 1b, and 1c show that the simulated mean flows are very similar. The only somewhat notable differences are 1) that the CROCO surface velocity tends to be slightly higher, 2) that the CROCO surface temperature tends to be slightly lower, and 3) that the CROCO pycnocline entrainment is weaker. The last point can be seen more clearly in figure 3. The CROCO runs produced weaker mixed-layer deepening although figure 1d suggests that CROCO runs had either a similar or more amount of energy flux reaching the mixed-layer base. (That is, the normalized buoyancy frequency of the pycnocline tends to be smaller for the CROCO runs while the dimensional N^2 of the pycnocline is the same for both NCAR and CROCO runs. This is a result of a slightly larger $\overline{u}_0$ in the CROCO runs, which leads to a larger U_E, a deeper z_w, and a smaller $z_w - z_p$, a larger E_b, and a larger Γ_N.) Furthermore, despite the slower mixed-layer deepening in the CROCO runs, CROCO tends to have a slightly stronger resolved buoyancy flux at the mixed-layer base (figure 1e). This implies that the NCAR's faster entrainment occurs because NCAR's explicit SGS diffusion is larger than CROCO's implicit SGS (that is, only numerical) diffusion. This point is demonstrated later in section 2.2 where we add explicit SGS diffusion terms to a CROCO run.

Figures 1e, 1f, 2a, 2b, 2c, 2e, and 2f show that the resolved turbulence statistics are overall very similar. Note that a difference of up to about 10 % should be considered negligible for the domain size used and the time window lengths used for averaging because this level of difference occurs even due to a change of the time step length, which causes different realization of instantaneous chaotic turbulent flow without altering the turbulence statistics (appendix **??**). Especially, the profiles of $\overline{w'w'w'}$, $\overline{v'w'}$, and $\overline{b'b'}$ fluctuate largely and require a large sample size to obtain a well-sampled profile. Our sample size is not yet large enough to reach such a well-sampled profile for these quantities, and some levels of differences are merely due to the insufficient sample size. However, near the surface where the turbulence structures tend to be small, the statistics are more robust even for these quantities. Despite the limited sample size, we can still robustly see that the resolved turbulence quantities near the surface tend to be stronger for the CROCO runs. This stronger resolved turbulence is closely related to the difference in the SGS parameterization, which becomes significant near the surface. Generally, a stronger SGS diffusion tends to weaken the resolved turbulence. Therefore, the result here implies that the CROCO's numerical diffusion is weaker than the explicit SGS diffusion of the NCAR model. As shown in section 2.2, the difference in the resolved turbulence quantities significantly reduces when the CROCO model uses an explicit SGS diffusion additionally to the (unavoidable) numerical diffusion.

Figures 2c and 2d show that the variances of the resolved w and b in the stratified part of the water ($z/|z_p| \lesssim -0.9$) tend to be larger with the NCAR model. This is partially due to the slightly smaller U_E and E_b in the NCAR runs. However, this tendency persists in the dimensional variances as well. Contrary to these variances, the resolved buoyancy flux (figure 1e) at the same depths tends to be less with the NCAR model. Therefore, the NCAR runs have stronger internal waves (who have no buoyancy flux when they are not growing nor decaying) and less resolved turbulent mixing.

To further investigate this difference, the spectra of 1D discrete FFT modes and the circularly-integrated 2D energy spectra of u', v', w', and b' are shown in figures 4 and 5. These spectra are taken from three different regions: namely, the mixed-layer interior ($-32\,\mathrm{m} < z < -6\,\mathrm{m}$), the entrainment layer ($-60\,\mathrm{m} < z < -38\,\mathrm{m}$), and the pycnocline interior ($-132\,\mathrm{m} < z <$

$-70\,\mathrm{m}$). Overall, the NCAR and CROCO simulations tend to differ at the spectral heads and tails. These figures are made using the data taken from special runs having a larger horizontal domain size of $640\,\mathrm{m} \times 640\,\mathrm{m}$ to have more wavenumbers and for better statistics, and the results are very similar to the baseline domain size of $320\,\mathrm{m} \times 320\,\mathrm{m}$. The CROCO run here uses the sound speed $c_s = 3\,\mathrm{m\,s^{-1}}$ and the second viscosity $\lambda = 1\,\mathrm{kg\,s^{-1}\,m^{-1}}$, and the results are very similar to those with $c_s = 202\,\mathrm{m\,s^{-1}}$. We show only the spectra from the case with $(U_*, Q_*) = (0.012\,\mathrm{m\,s^{-1}}, 5\,\mathrm{W\,m^{-2}})$ because the differences between the NCAR and CROCO simulations have similar tendency for all other cases.

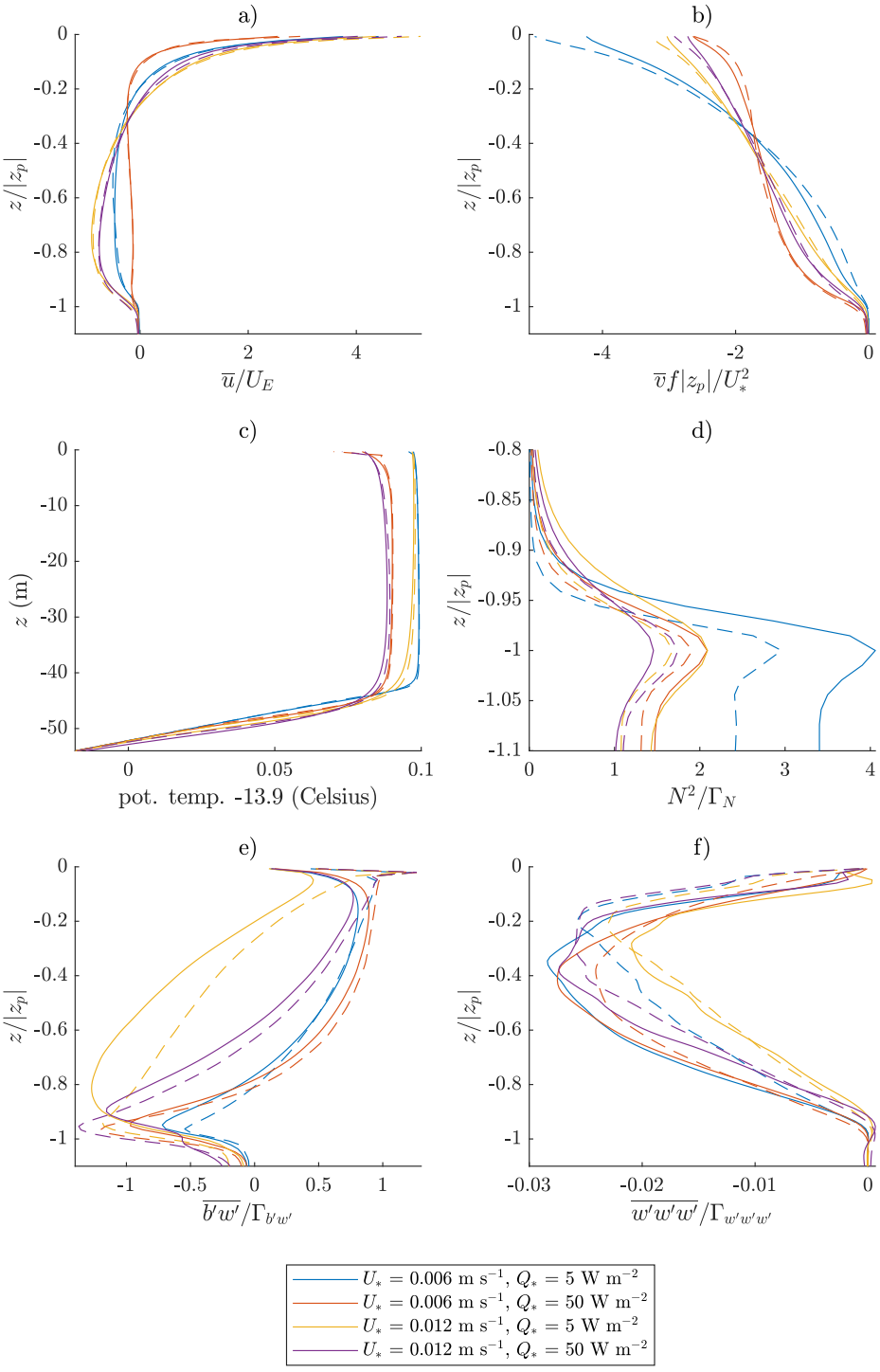

Figure 1. Comparison between the NCAR LES model (solid) and the CROCO NBQ model (dashed). The line color indicates the surface forcing as shown in the legend.

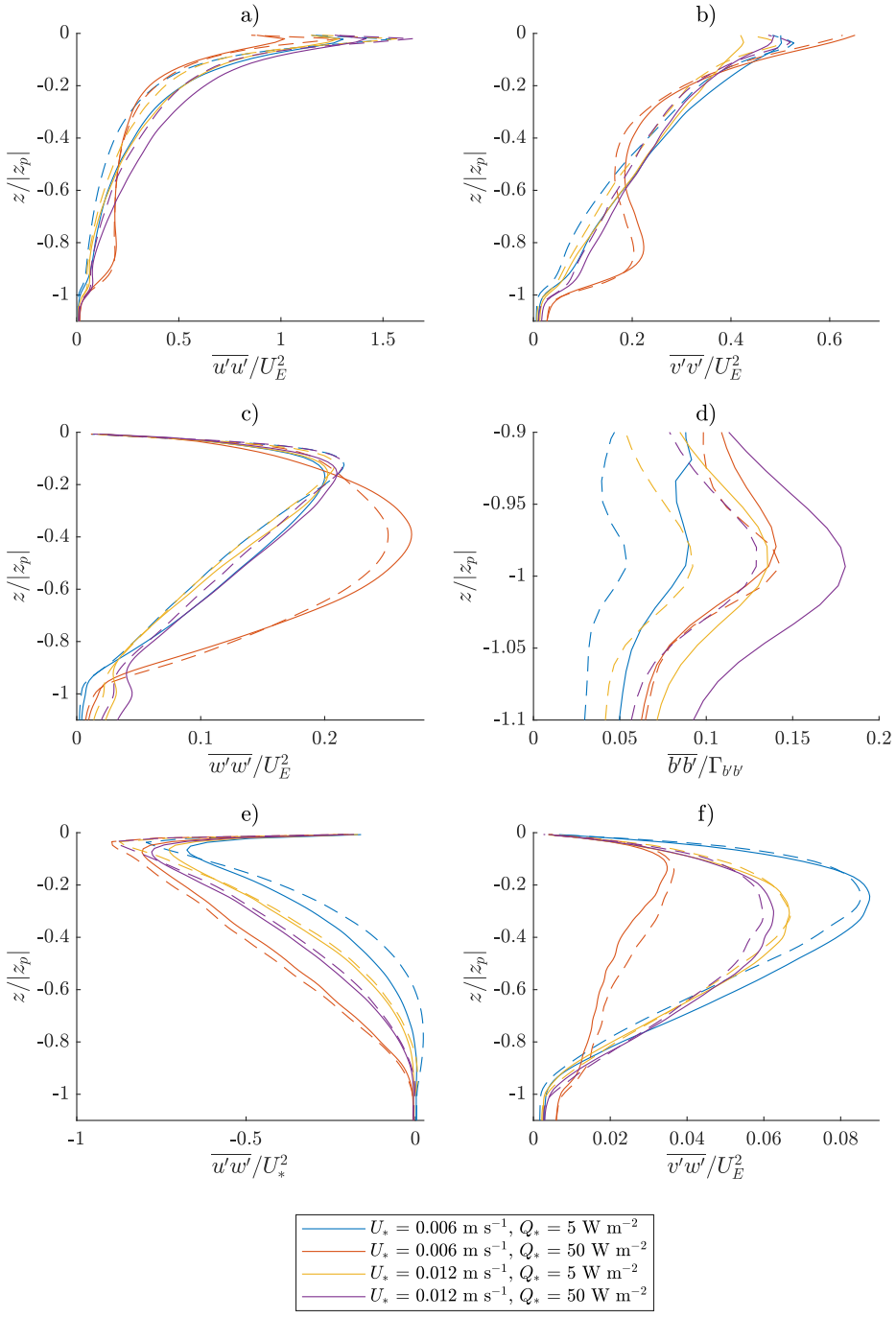

Figure 2. Comparison between the NCAR LES model (solid) and the CROCO NBQ model (dashed). The line color indicates the surface forcing as shown in the legend.

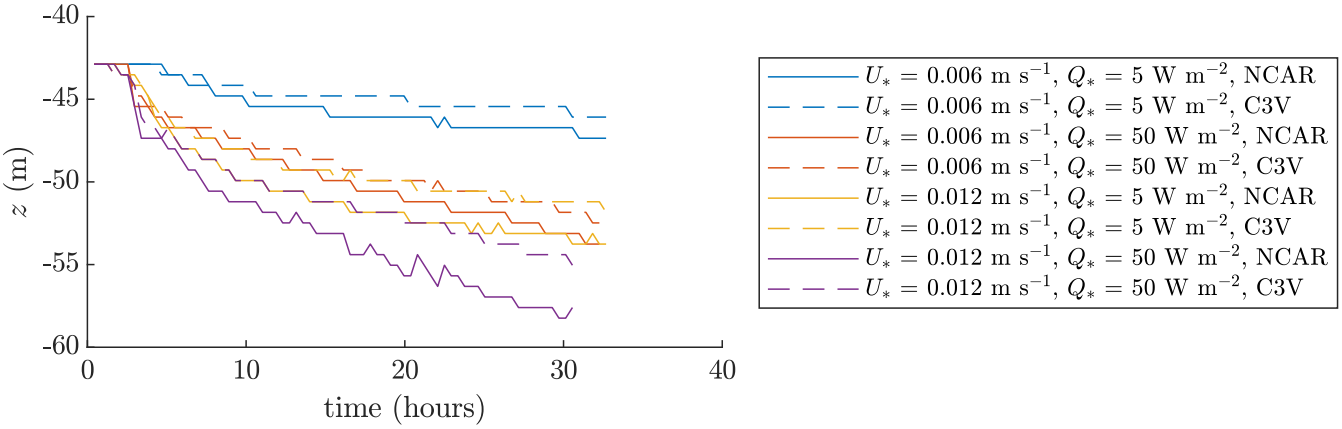

Figure 3. Time series of the mixed-layer-base depth z_p. C3V in the legend refers to the CROCO NBQ run with the sound speed $c_s = 3\,\mathrm{m\,s^{-1}}$ and the second viscosity $\lambda = 1\,\mathrm{kg\,s^{-1}\,m^{-1}}$. The difference in the mixed-layer deepening occurs mainly because NCAR's explicit SGS diffusion is larger than CROCO's implicit SGS (that is, only numerical) diffusion.

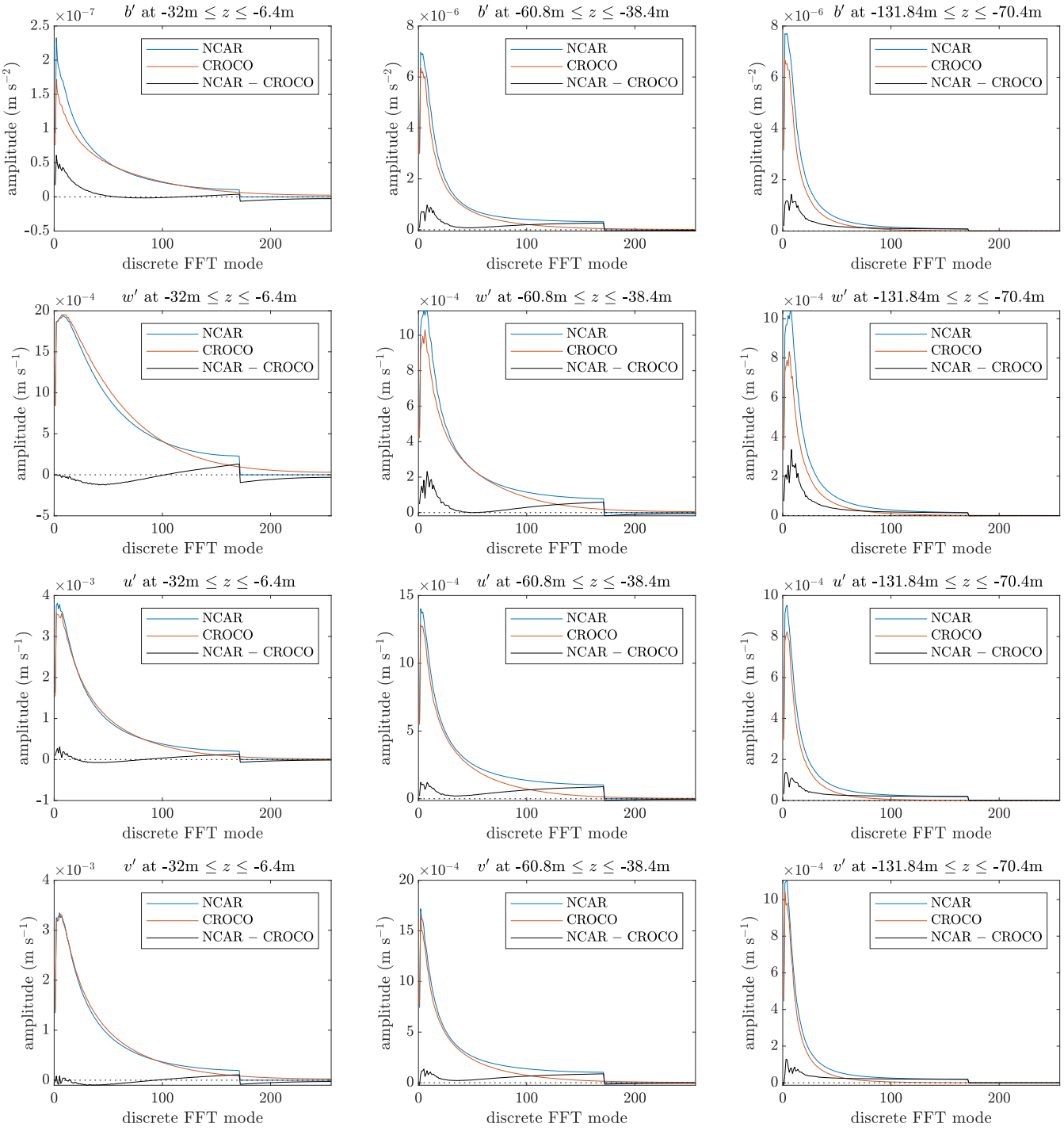

Figure 4. Comparison of the 1D discrete FFT spectra with $(U_*, Q_*) = (0.012\,\mathrm{m\,s^{-1}}, 5\,\mathrm{W\,m^{-2}})$. Each spectrum is smoothed by averaging over the vertical range shown in each title as well as averaging over 21 hours and each horizontal direction.

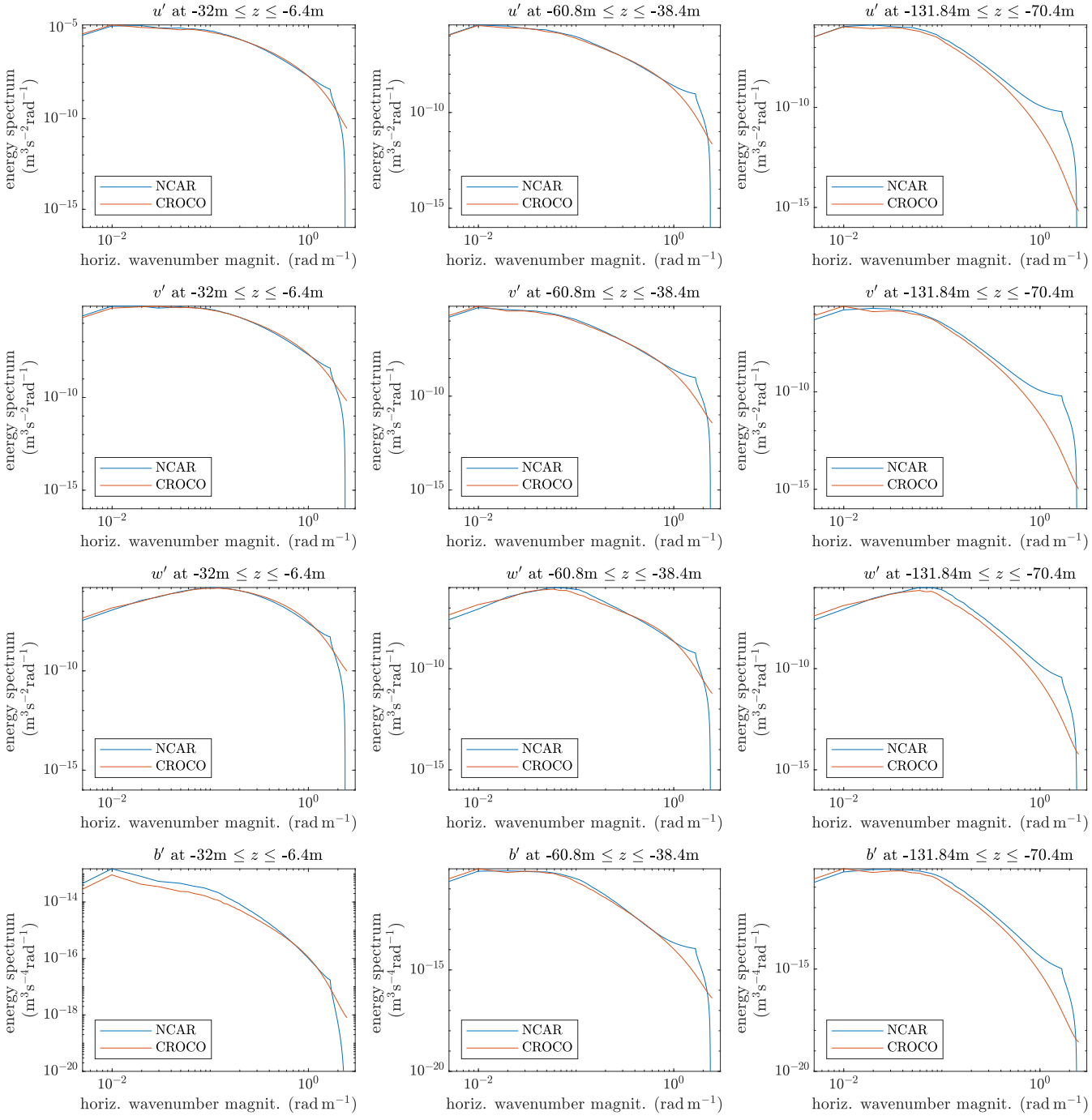

Figure 5. Comparison of the 2D spectra averaged in circular rings at constant horizontal wavenumber magnitude from the runs with $(U_*, Q_*) = (0.012\,\mathrm{m\,s^{-1}}, 5\,\mathrm{W\,m^{-2}})$. Each spectrum is smoothed by averaging over the vertical range shown in each title as well as averaging over 21 hours.

2.2 The effect of the explicit SGS parameterization

This subsection shows how explicit SGS diffusion terms affect the results in subsection 2.1. For this, we focus on the case with $(U_*, Q_*) = (0.012\,\mathrm{m\,s^{-1}}, 50\,\mathrm{W\,m^{-2}})$ because this case has the largest difference in the mixed-layer deepening, which is the most significant difference observed in the previous subsection.

Here, the CROCO NBQ run uses a modified version of the SGS parameterization by Lilly (1962).

$$\tau_{ih} = \nu_H \left(\frac{\partial u_i}{\partial x_h} + \frac{\partial u_h}{\partial x_i} \right), \tag{13}$$

$$\tau_{i3} = \nu_V \left(\frac{\partial u_i}{\partial z} + \frac{\partial w}{\partial x_i} \right), \tag{14}$$

$$\tau_{\theta h} = \mathrm{Pr}\, \nu_H \frac{\partial \theta}{\partial x_h}, \tag{15}$$

$$\tau_{\theta z} = \mathrm{Pr}\, \nu_V \frac{\partial \theta}{\partial z}, \tag{16}$$

where

$$S_{ij} = \frac{1}{2} \left(\frac{\partial u_i}{\partial x_j} + \frac{\partial u_j}{\partial x_i} \right), \tag{17}$$

$$D = \sqrt{2 S_{ij} S_{ij}}, \tag{18}$$

$$\nu_H = C_s^2 \Delta x \Delta y D \sqrt{\max\left(0,\, 1 - \frac{N^2/D^2}{C_R}\right)}, \tag{19}$$

$$\nu_V = C_s^2 \Delta z \Delta z D \sqrt{\max\left(0,\, 1 - \frac{N^2/D^2}{C_R}\right)}, \tag{20}$$

and the indexes are $h = 1, 2$, $i = 1, 2, 3$, and $j = 1, 2, 3$, and the summation convention is used, and the model parameters are the Smagorinsky constant C_s, Prandtl number Pr, and a mixing-threshold constant C_R. The SGS terms become zero when a Richardson-like number N^2/D^2 exceeds C_R. As mentioned in the introduction of section 2, the NCAR model's SGS parameterization below $z = -21\,\mathrm{m}$ is roughly relatable to the Smagorinsky model with $C_s = 0.18$. Therefore, we test $C_s = 0.17$ and 0.2 with CROCO. These values of C_s together with a large value of Pr produce the mixed-layer deepening comparable to the NCAR model run as shown in figure 6 where the mixed-layer deepening with (C_s, C_R, Pr) = (0.17, 0.25, 3) and (0.2, 1, 4) are shown. This result demonstrates that the difference in the mixed-layer deepening seen in the previous subsection is due to the SGS parameterization, and the numerical diffusion of the CROCO runs is less than the combined amount of the numerical and explicit diffusion of the NCAR model.

The previous subsection also showed that the resolved turbulence quantities near the surface tend to be larger with the CROCO model without an explicit SGS parameterization. This difference also significantly reduces with the addition of the explicit SGS parameterization as shown in figures 7 and 8.[6] This is because a stronger diffusion weakens the resolved turbulence. There are some small remaining differences, but they are expected because different explicit SGS parameterizations are used in the NCAR and CROCO models.

[6] Each profile is an average of 21 samples taken every one-fortieth of the inertial period during $t = 4.7$ to 13.6 hours.

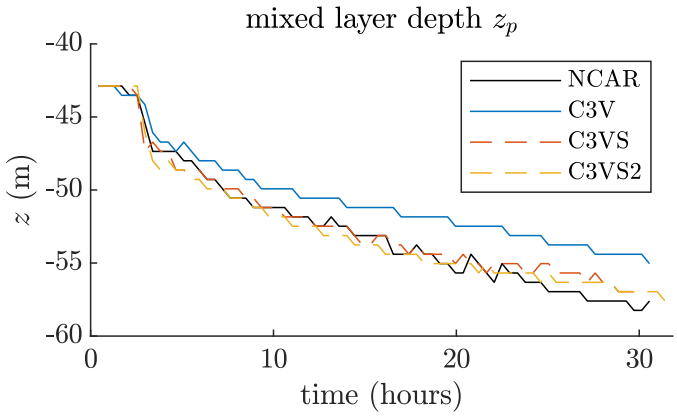

Figure 6. Time series of the mixed-layer-base depth z_p. The CROCO NBQ runs (C3V, C3VS, C3VS2 in the legend) use the sound speed $c_s = 3\,\mathrm{m\,s^{-1}}$ and the second viscosity $\lambda = 1\,\mathrm{kg\,s^{-1}\,m^{-1}}$. C3V uses only numerical diffusion. C3VS and C3VS2 use an explicit SGS parameterization (13)-(20) with $(C_s, C_R, \mathrm{Pr}) = (0.17, 0.25, 3)$ and (0.2, 1, 4), respectively.

In summary, the NCAR results and the CROCO results are overall very comparable. There are some minor differences, but most of them are due to the different SGS parameterization. The only notable difference that may not be attributable to the SGS parameterization difference is that the NCAR model runs tend to produce more internal waves in the stratified part.

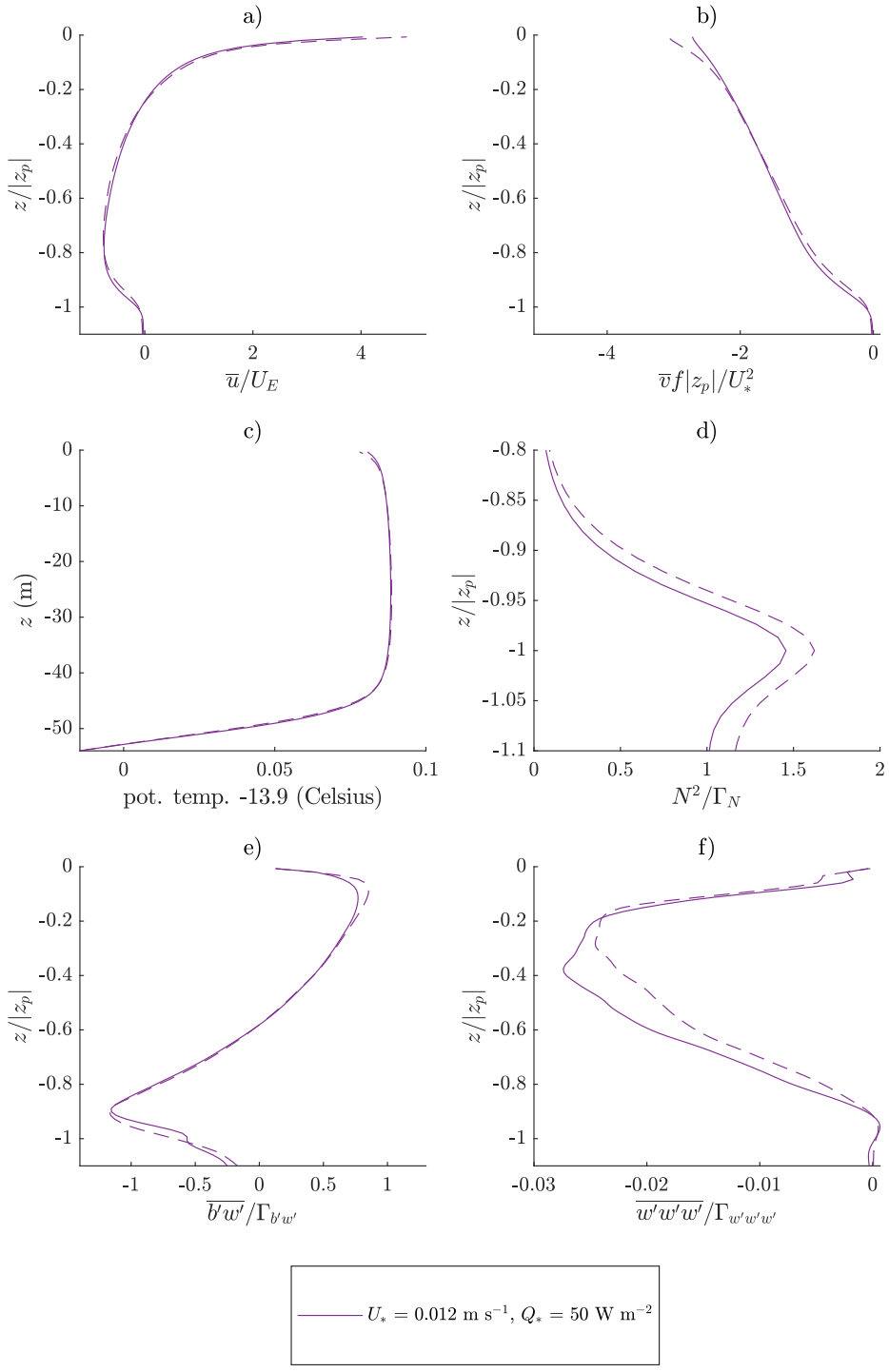

Figure 7. Comparison between the NCAR run (solid) and the CROCO run (dashed) with $(C_s, C_R, \mathrm{Pr}) = (0.17, 0.25, 3)$.

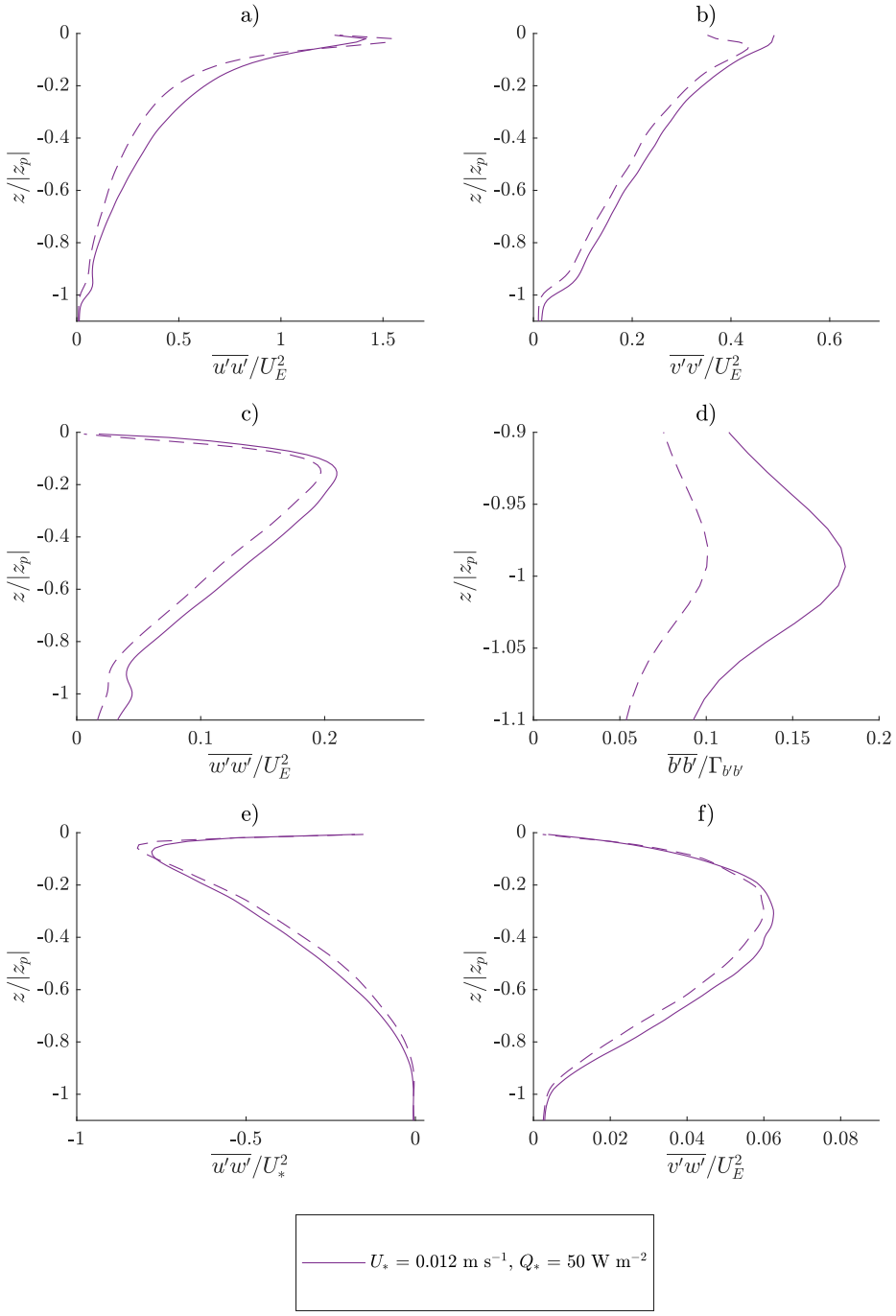

Figure 8. Comparison between the NCAR run (solid) and the CROCO run (dashed) with $(C_s, C_R, \mathrm{Pr}) = (0.17, 0.25, 3)$.

2.3 The effect of the second viscosity parameter

For the CROCO NBQ model runs, an unphysically-large value of the second viscosity λ may be used to aggressively dissipate (near-grid-scale) pseudo-acoustic waves and stabilize the simulation. Therefore, here we test whether an unphysically-large value of λ affects the turbulence statistics. The results show that the turbulence statistics are not affected.

We present two types of CROCO runs having the speed-of-sound parameter $c_s = 202\,\mathrm{m\,s^{-1}}$. One type (referred to as C202) uses $\lambda = 0.01\,\mathrm{kg\,s^{-1}\,m^{-1}}$, and the other type (referred to as C202V) uses $\lambda = 19\,\mathrm{kg\,s^{-1}\,m^{-1}}$ for $(U_*, Q_*) = (0.006\,\mathrm{m\,s^{-1}}, 50\,\mathrm{W\,m^{-2}})$ and $\lambda = 18\,\mathrm{kg\,s^{-1}\,m^{-1}}$ for all other values of (U_*, Q_*). Figures 9 and 10[7] show the flow statistics from C202 and C202V are essentially identical.

By increasing λ, the optimal slow-mode time step increases from $0.15\,\mathrm{s}$ to $0.2\,\mathrm{s}$ for the case with $(U_*, Q_*) = (0.006\,\mathrm{m\,s^{-1}}$, $5\,\mathrm{W\,m^{-2}})$, and from $0.04\,\mathrm{s}$ to $0.08\,\mathrm{s}$ for the cases with $(U_*, Q_*) = (0.012\,\mathrm{m\,s^{-1}}$, $5\,\mathrm{W\,m^{-2}})$ and $(0.012\,\mathrm{m\,s^{-1}}$, $50\,\mathrm{W\,m^{-2}})$. However, for the case with $(U_*, Q_*) = (0.006\,\mathrm{m\,s^{-1}}$, $50\,\mathrm{W\,m^{-2}})$, increasing λ does not lead to an increase of the slow-mode time, which stays at $0.25\,\mathrm{s}$. The optimal fast-mode time step is unaffected by λ and is about $0.0038\,\mathrm{s}$ for all values of (U_*, Q_*). Therefore, increasing λ speeds up the simulations only moderately.

[7] The initial conditions for the C202 and C202V runs are prepared by simulating the boundary layers for 4 hours using $c_s = 3\,\mathrm{m\,s^{-1}}$ and $\lambda = 1\,\mathrm{kg\,s^{-1}\,m^{-1}}$ from a quiescent state. The boundary layers fully develop during this time. At the time of the initial conditions, we reset $t = 0\,\mathrm{s}$, $c_s = 202\,\mathrm{m\,s^{-1}}$, and λ to the new values. Every profile from $(U_*, Q_*) = (0.006\,\mathrm{m\,s^{-1}}$, $5\,\mathrm{W\,m^{-2}})$, $(0.006\,\mathrm{m\,s^{-1}}$, $50\,\mathrm{W\,m^{-2}})$, $(0.012\,\mathrm{m\,s^{-1}}$, $5\,\mathrm{W\,m^{-2}})$, and $(0.012\,\mathrm{m\,s^{-1}}$, $50\,\mathrm{W\,m^{-2}})$ is an average of the samples taken every one-fortieth of the inertial period during $t =$ 4-7, 2.5-5.5, 2-11, and 2-11 hours, respectively.

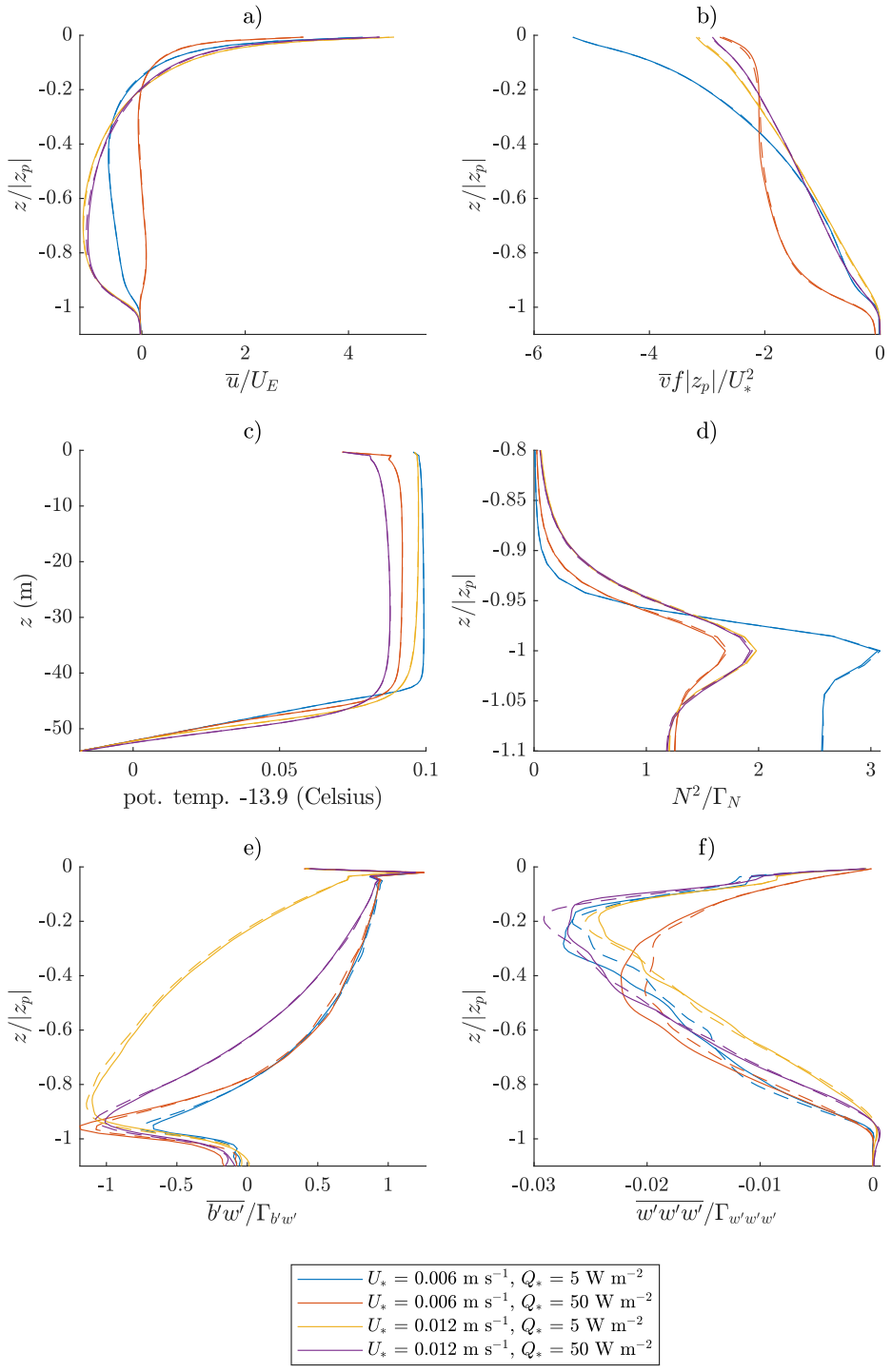

Figure 9. The effect of the second viscosity λ. The C202 runs (solid) use $\lambda = 0.01\,\mathrm{kg\,s^{-1}\,m^{-1}}$, and the C202V runs (dashed) use $\lambda = 18\,\mathrm{kg\,s^{-1}\,m^{-1}}$ to $19\,\mathrm{kg\,s^{-1}\,m^{-1}}$.

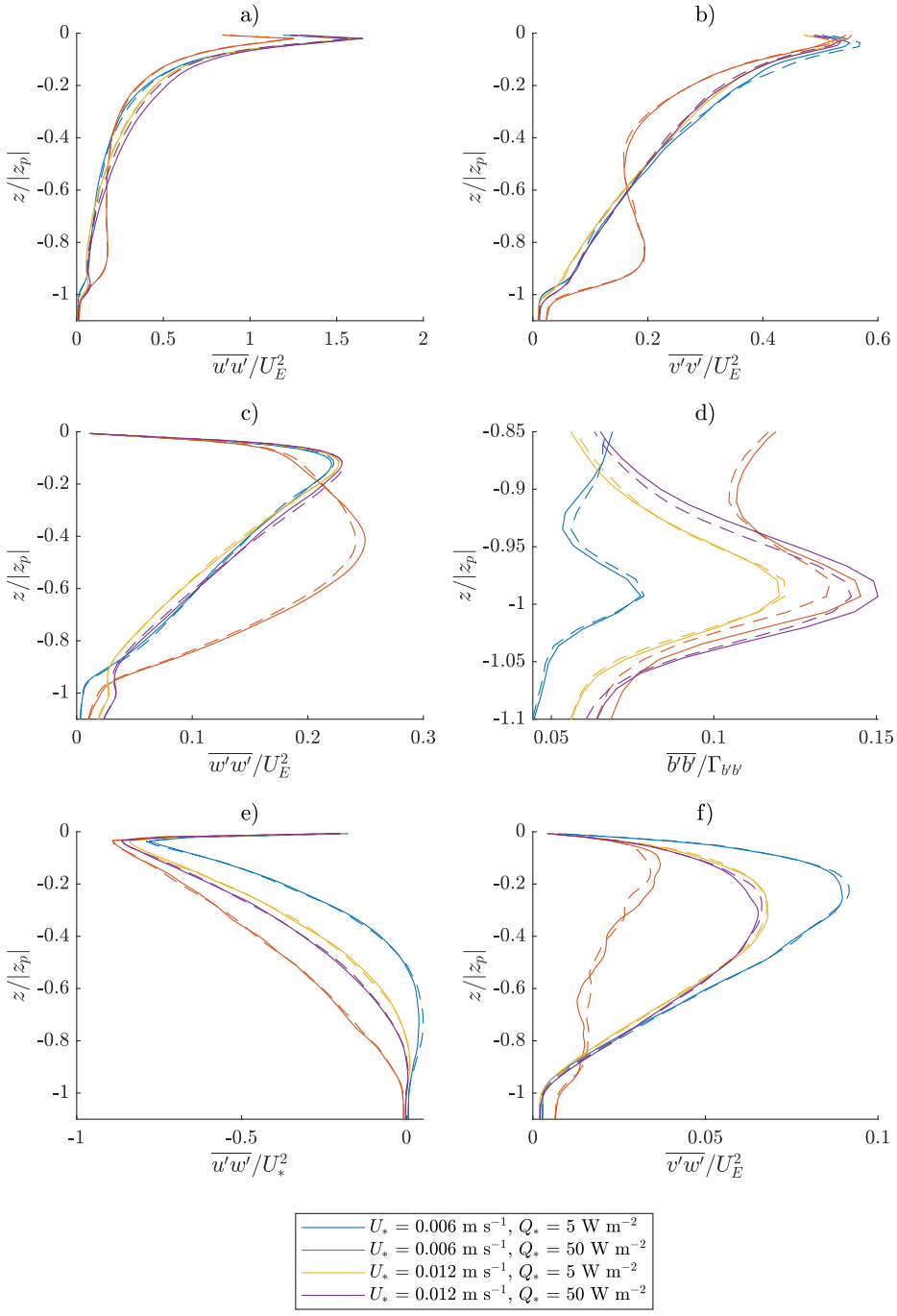

Figure 10. The effect of the second viscosity λ. The C202 runs (solid) use $\lambda = 0.01\,\mathrm{kg\,s^{-1}\,m^{-1}}$, and the C202V runs (dashed) use λ=18 $\mathrm{kg\,s^{-1}\,m^{-1}}$ to 19 $\mathrm{kg\,s^{-1}\,m^{-1}}$.

2.4 Sensitivity to the speed-of-sound parameter

Reducing the speed-of-sound parameter c_s in the CROCO NBQ model allows a larger time step by relaxing the CFL condition related to pseudo-acoustic waves. Here, we study the effect of reducing the value of c_s to a very small value, $c_s = 3\,\mathrm{m\,s^{-1}}$. The results show that the resolved turbulence statistics are largely insensitive to the value of c_s. However, it should be noted that c_s should not be smaller than the fastest speed of the process that needs to be properly simulated, for example, the barotropic wave speed in the case of geophysical applications.

Figures 11 and 12[8] compare two types of CROCO runs: one (referred to as C3V) uses $c_s = 3\,\mathrm{m\,s^{-1}}$ and the second viscosity $\lambda = 1\,\mathrm{kg\,s^{-1}\,m^{-1}}$, and the other (referred to as C202) uses $c_s = 202\,\mathrm{m\,s^{-1}}$ and $\lambda = 0.01\,\mathrm{kg\,s^{-1}\,m^{-1}}$. Most profiles in these figures show only small differences that should be considered negligible for the given limited domain size. The only possibly non-negligible difference appears in the internal wave strength seen below $z/|z_p| \approx -0.9$ in figures 12c and 12d for the cases with $U_* = 0.012\,\mathrm{m\,s^{-1}}$.

By decreasing c_s together with increasing λ, the optimal slow-mode and fast-mode time steps increase to $0.5\,\mathrm{s}$ and $0.019\,\mathrm{s}$, respectively, for all C3V runs.[9] Therefore, compared to the C202 runs, C3V runs are more than 5 times faster.

[8] Every profile from $(U_*, Q_*) = (0.006\,\mathrm{m\,s^{-1}},\ 5\,\mathrm{W\,m^{-2}})$, $(0.006\,\mathrm{m\,s^{-1}},\ 50\,\mathrm{W\,m^{-2}})$, $(0.012\,\mathrm{m\,s^{-1}},\ 5\,\mathrm{W\,m^{-2}})$, and $(0.012\,\mathrm{m\,s^{-1}},\ 50\,\mathrm{W\,m^{-2}})$ is an average of the samples taken every one-fortieth of the inertial period during a time window of 3, 4.5, 9, and 9 hours starting from 4, 2, 2, and 2 hours, respectively, after the simulations' initial conditions. The initial conditions are made by simulating the boundary layer for 4 hours by C3V. The boundary layer fully develops in 4 hours from a quiescent state.

[9] Decreasing c_s without increasing λ makes simulations unstable. Therefore, it is not recommendable.

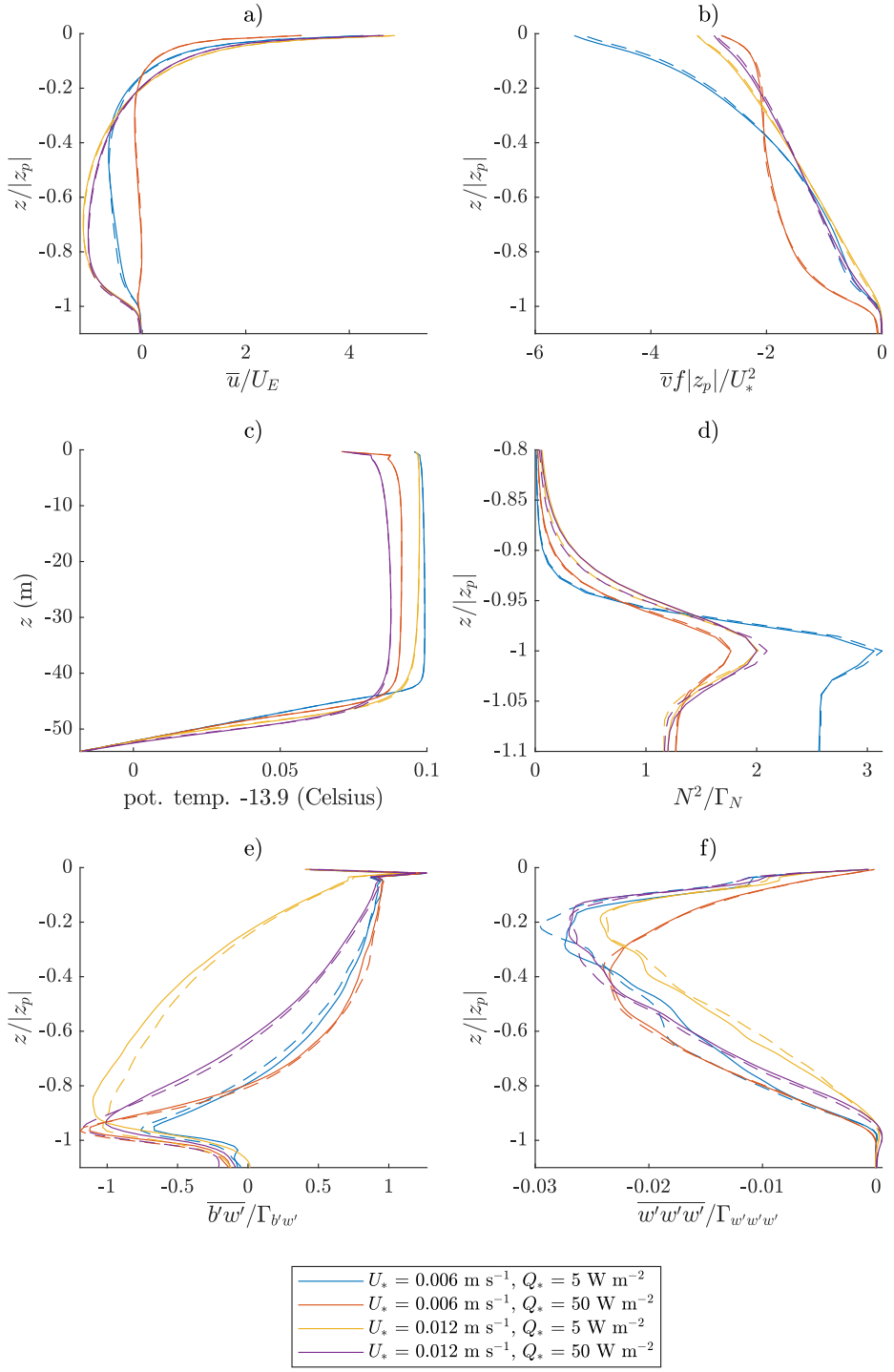

Figure 11. The effect of the speed-of-sound parameter c_s. The solid lines are with $c_s = 202\,\mathrm{m\,s^{-1}}$, and the dashed lines are with $c_s = 3\,\mathrm{m\,s^{-1}}$.

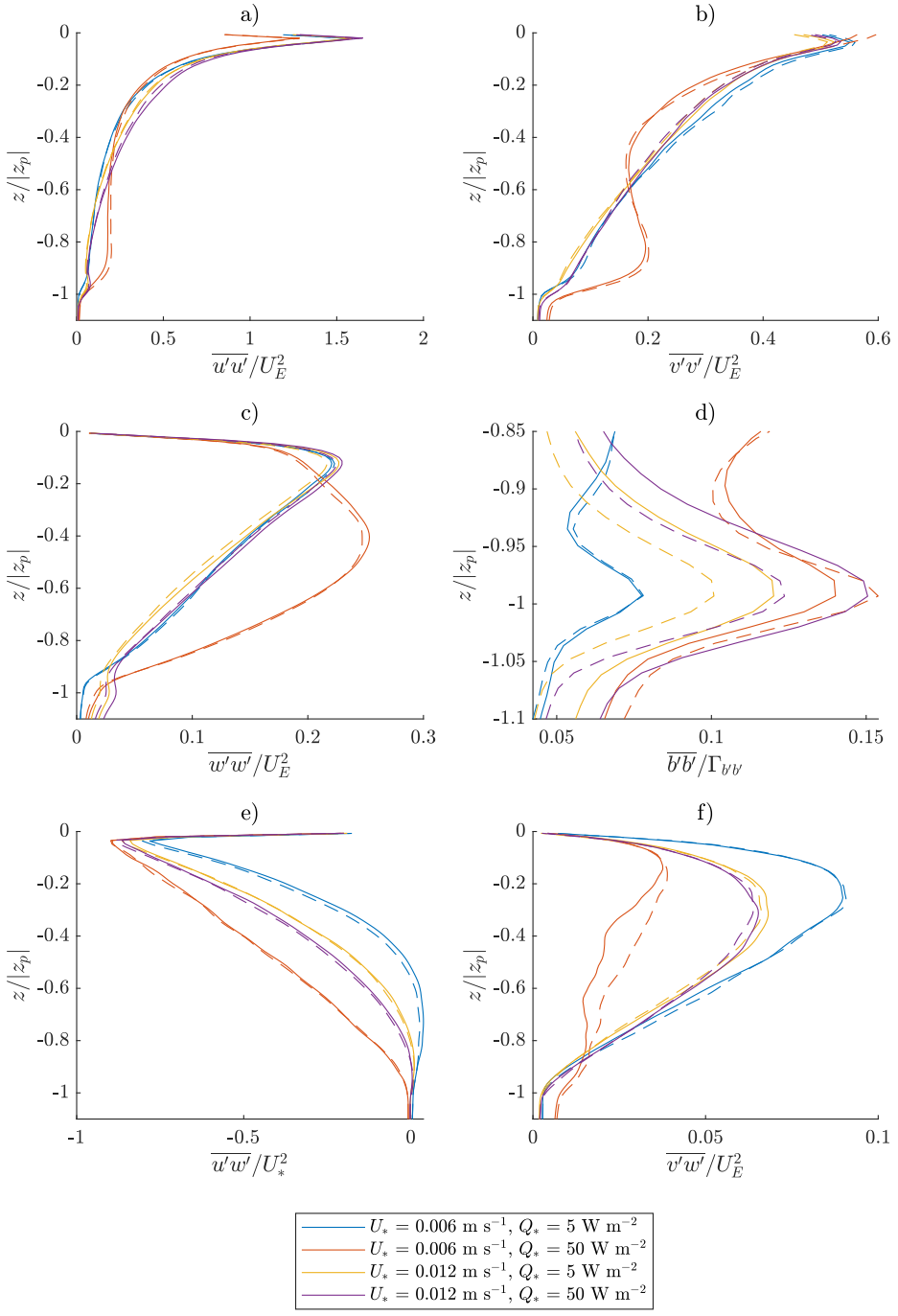

Figure 12. The effect of the speed-of-sound parameter c_s. The solid lines are with $c_s = 202\,\mathrm{m\,s^{-1}}$, and the dashed lines are with $c_s = 3\,\mathrm{m\,s^{-1}}$.

3 Efficiency comparison

Many factors have influence on the model computing efficiency, such as the structure of the computing platform, Message Passing Interface (MPI) parallelisation, 2D-decomposition of the models, etc.

3.1 Computing platform tests

The number and allocation of nodes and processors used for computing and the availability of threads matter the efficiency of model operations. In this study, the Cheyenne supercomputer is used for efficiency tests. The Cheyenne supercomputer built for NCAR operates as one of the world's most energy-efficient and high-performance computers. The simulations involved in this paper are all for exclusive use of the nodes. In each efficiency test, the number of nodes, the number of CPU per node, the number of MPI processes and the number of OpenMP threads can be specified.

Combinations of nodes and CPUs per node with different problem sizes and the total number of processors were tested (Figure xxx). In the same case of the problem size and total number of processors, the combination of more nodes and less CPUs per node makes the model compute more efficiently. However, the selection of nodes and CPUs per node is better to stick to affordable and moderate numbers instead of extreme disparity of them, because more nodes requested to Cheyenne let the submitted job stay in the waiting queue before running longer, though computing time is shorter.

3.2 Model computing optimization

3.2.1 CROCO MPI parallelisation

CROCO is currently supported by two kinds of parallelism, MPI and OpenMP, which respectively represent distributed memory and shared memory. Based on the settings of computing platform, the awareness of CROCO MPI and OpenMP settings is necessary to be defined as needed. According to the Table xxx, when the OpenMP is undefined in CROCO CPP keys, the computing time with or without OpenMP thread of Cheyenne system can be treated as the same, which means the awareness of OpenMP of the model determine the usage of threads in the simulation. In this paper, CROCO is used with undefined OpenMP and defined MPI, which means only one thread is used for each processor of Cheyenne computer, and the decomposition of processors impact the computing efficiency.

NP_XI and NP_ETA in CROCO represents the MPI decomposition in XI and ETA direction respectively. In order to match the number of processors used in Cheyenne, the product of NP_XI and NP_ETA should be as the same as the product of the number of nodes and the number of CPU per node. Different combinations of NP_XI and NP_ ETA are tested under the frameworks of different combinations of problem size and total number of processors in the Cheyenne environment.

3.2.2 NCAR-LES 2D-decomposition

3.2.3 Results and discussion

The performance of the model efficiency for varying problem sizes and workload per processor is shown from Figure 13 to Figure 15. NP = $NP_z \times NP_{xy}$ where NP_z and NP_{xy} are respectively the number of processors in the vertical and horizontal directions. In each figure, the vertical axis is the computing time for each time step t multiplied by NP and divided by total work size. N_z is the number of vertical levels and $M_{x,y} = N_{x,y}\ \log N_{x,y}$ with $N_{x,y}$ the number of grid points in the x and y directions.

Figure 13 shows the computational time per grid point for different combinations of problem size (an example of strong scaling). For a given number of total processors NP, the symbol is the most optimal combination of MPI parallelisation or 2D decomposition. Figure 14 and 15 shows computational time per grid point for a fixed amount of work per processor (an example of weak scaling). The different numbers of barotropic time-steps between each baroclinic time step (NDTFAST) have great influence on computing efficiency.

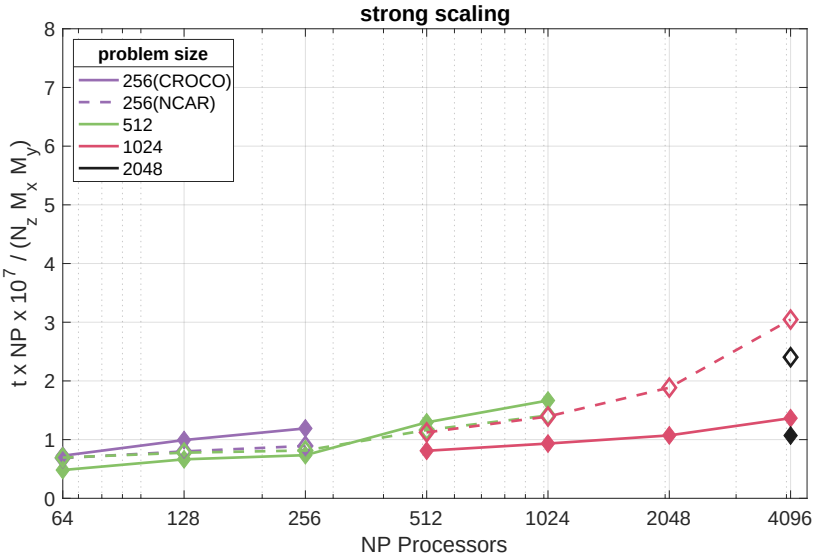

Figure 13. Computational time per grid point for different combinations of problem size for CROCO and NCAR-LES (an example of strong scaling). a) purple lines and symbols problem size 256^3; b) green lines and symbols 512^3; c) red lines and symbols 1024^3; and d) black symbol 2048^3.

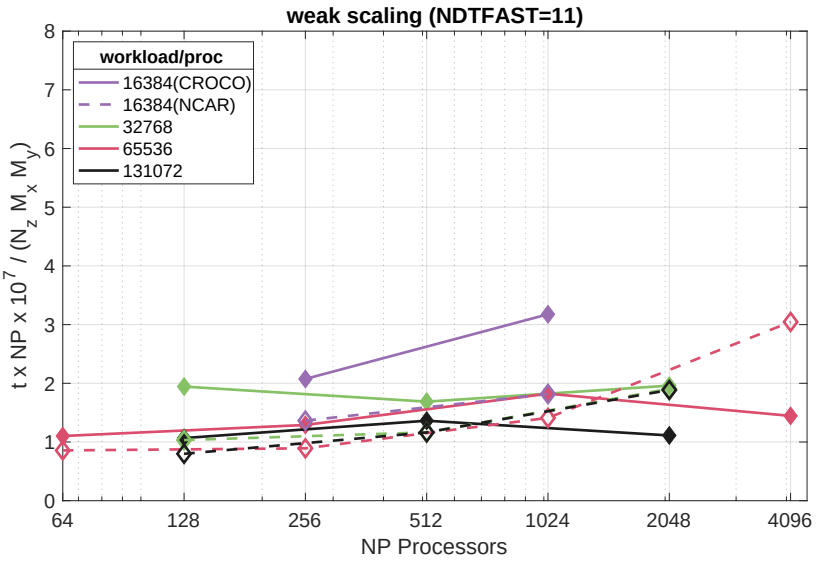

Figure 14. Computational time per grid point for a fixed amount of work per processor (an example of weak scaling) with NDTFAST=11.

4 Conclusions

- CROCO performs well in the non-hydrostatic simulations with the horizontal and vertical resolution of 1 meter;
- CROCO turbulence is slightly less intense for the same wind and surface cooling forcing than the NCAR-LES;
- CROCO parameterizations impact the simulation accuracy results;
- In efficiency comparisons, the computing time of CROCO model is different but comparable with NCAR-LES model;
- CROCO MPI parallelization and NCAR-LES 2D decomposition impact the model's efficiency.

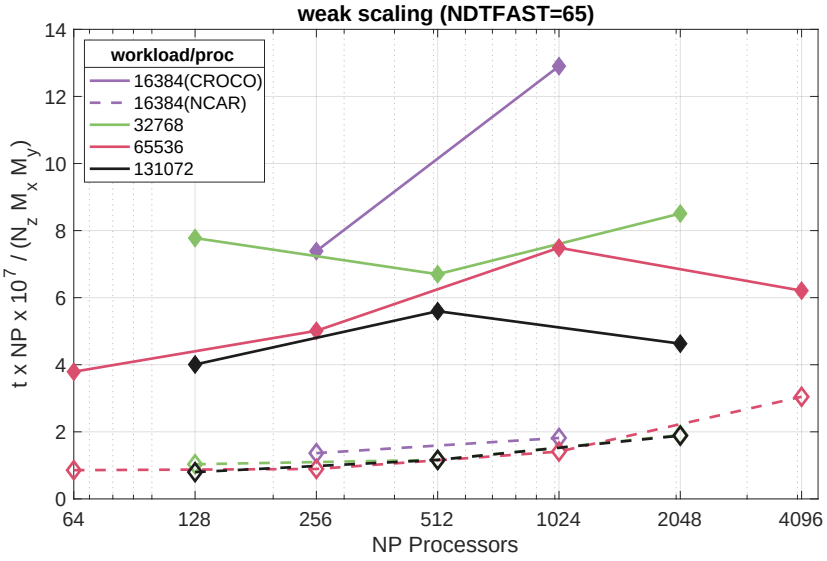

Figure 15. Computational time per grid point for a fixed amount of work per processor (an example of weak scaling) with NDTFAST=65.

Acknowledgements. The existing accuracy comparison part of this article is mainly done by Nobuhiro Suzuki. The additional accuracy comparison part completed by Xiaoyu Fan will be added later.

References

Auclair, F., Bordois, L., Dossmann, Y., Duhaut, T., Paci, A., Ulses, C., and Nguyen, C.: A non-hydrostatic non-Boussinesq algorithm for free-surface ocean modelling, Ocean Modelling, 132, 12–29, https://doi.org/https://doi.org/10.1016/j.ocemod.2018.07.011, 2018.

Beets, C. and Koren, B.: Large-eddy simulation with accurate implicit subgrid-scale diffusion, Department of Numerical Mathematics Rep., NM-R9601, pp. 24, 1996.

Borges, R., Carmona, M., Costa, B., and Don, W. S.: An improved weighted essentially non-oscillatory scheme for hyperbolic conservation laws, Journal of Computational Physics, 227, 3191–3211, https://doi.org/https://doi.org/10.1016/j.jcp.2007.11.038, 2008.

Debreu, L., Auclair, F., Benshila, R., Capet, X., Dumas, F., Julien, S., and Marchesiello, P.: Multiresolution in CROCO (Coastal and Regional Ocean Community model), in: EGU General Assembly Conference Abstracts, pp. EPSC2016–15 272, 2016.

Fox, D. G. and Orszag, S. A.: Pseudospectral approximation to two-dimensional turbulence, Journal of Computational Physics, 11, 612–619, https://doi.org/https://doi.org/10.1016/0021-9991(73)90141-1, 1973.

Li, Q. and Fox-Kemper, B.: Assessing the Effects of Langmuir Turbulence on the Entrainment Buoyancy Flux in the Ocean Surface Boundary Layer, Journal of Physical Oceanography, 47, 2863 – 2886, https://doi.org/10.1175/JPO-D-17-0085.1, 2017.

Lilly, D. K.: On the numerical simulation of buoyant convection, Tellus, 14, 148–172, https://doi.org/10.3402/tellusa.v14i2.9537, 1962.

Marchesiello, P., Auclair, F., Debreu, L., McWilliams, J., Almar, R., Benshila, R., and Dumas, F.: Tridimensional nonhydrostatic transient rip currents in a wave-resolving model, Ocean Modelling, 163, 101 816, https://doi.org/https://doi.org/10.1016/j.ocemod.2021.101816, 2021.

Marshall, J., Hill, C., Perelman, L., and Adcroft, A.: Hydrostatic, quasi-hydrostatic, and nonhydrostatic ocean modeling, Journal of Geophysical Research: Oceans, 102, 5733–5752, 1997.

Moeng, C.-H.: A Large-Eddy-Simulation Model for the Study of Planetary Boundary-Layer Turbulence, Journal of Atmospheric Sciences, 41, 2052 – 2062, https://doi.org/10.1175/1520-0469(1984)041<2052:ALESMF>2.0.CO;2, 1984.

Orszag, S. A.: On the Elimination of Aliasing in Finite-Difference Schemes by Filtering High-Wavenumber Components, Journal of Atmospheric Sciences, 28, 1074 – 1074, https://doi.org/10.1175/1520-0469(1971)028<1074:OTEOAI>2.0.CO;2, 1971.

Sullivan, P., McWilliams, J., and Moeng, C.: A subgrid-scale model for large-eddy simulation of planetary boundary-layer flows, Boundary-Layer Meteorol, 71, 247 – 276, https://doi.org/10.1007/BF00713741, 1994.

Sullivan, P., McWilliams, J., and Moeng, C.: A grid nesting method for large-eddy simulation of planetary boundary-layer flows, Boundary-Layer Meteorol, 80, 167 – 202, https://doi.org/10.1007/BF00119016, 1996.

Sullivan, P. P. and Patton, E. G.: The Effect of Mesh Resolution on Convective Boundary Layer Statistics and Structures Generated by Large-Eddy Simulation, Journal of the Atmospheric Sciences, 68, 2395 – 2415, https://doi.org/10.1175/JAS-D-10-05010.1, 2011.